Computer Methods and Programs in Biomedicine 236 (2023) 107549

Contents lists available at ScienceDirect

Computer Methods and Programs in Biomedicine

journal homepage: www.elsevier.com/locate/cmpb

Hip joint load prediction using inverse bone remodeling with homogenized FE models: Comparison to micro-FE and influence of material modeling strategy

Sebastian Bachmann[a,*], Dieter H. Pahr[a,b], Alexander Synek[a]

[a] Institute of Lightweight Design and Structural Biomechanics, TU Wien, Gumpendorfer Straße 7, Vienna 1060, Austria
[b] Division Biomechanics, Karl Landsteiner University of Health Sciences, Dr. Karl-Dorrek-Straße 30, Krems 3500, Austria

ARTICLE INFO

Article history:
Received 24 November 2022
Revised 23 March 2023
Accepted 12 April 2023

Keywords:
Loading estimation
Loading history
Bone adaptation
Micro finite-element
Homogenized finite-element
Inverse remodeling

ABSTRACT

Background and objective: Measuring physiological loading conditions *in vivo* can be challenging, as methods are invasive or pose a high modeling effort. However, the physiological loading of bones is also imprinted in the bone microstructure due to bone (re)modeling. This information can be retrieved by inverse bone remodeling (IBR). Recently, an IBR method based on micro-finite-element (µFE) modeling was translated to homogenized-FE (hFE) to decrease computational effort and tested on the distal radius. However, this bone has a relatively simple geometry and homogeneous microstructure. Therefore, the objective of this study was to assess the agreement of hFE-based IBR with µFE-based IBR to predict hip joint loading from the head of the femur; a bone with more complex loading as well as more heterogeneous microstructure.

Methods: hFE-based IBR was applied to a set of 19 femoral heads using four different material mapping laws. One model with a single homogeneous material for both trabecular and cortical volume and three models with a separated cortex and either homogeneous, density-dependent inhomogeneous, or density and fabric-dependent orthotropic material. Three different evaluation regions (full bone, trabecular bone only, head region only) were defined, in which IBR was applied. µFE models were created for the same bones, and the agreement of the predicted hip joint loading history obtained from hFE and µFE models was evaluated. The loading history was discretized using four unit load cases.

Results: The computational time for FE solving was decreased on average from 500 h to under 1 min (CPU time) when using hFE models instead of µFE models. Using more information in the material model in the hFE models led to a better prediction of hip joint loading history. Inhomogeneous and inhomogeneous orthotropic models gave the best agreement to µFE-based IBR (RMSE% $<$14%). The evaluation region only played a minor role.

Conclusions: hFE-based IBR was able to reconstruct the dominant joint loading of the femoral head in agreement with µFE-based IBR and required considerably lower computational effort. Results indicate that cortical and trabecular bone should be modeled separately and at least density-dependent inhomogeneous material properties should be used with hFE models of the femoral head to predict joint loading.

1. Introduction

Obtaining physiological loading conditions of joints is required for a multitude of problems. For example, to obtain safety factors for fracture risk analysis [1], to obtain loading conditions for testing of implants [2], to infer habitual activities of extinct living beings [3], or to enhance patient-specific models [4,5]. But, obtaining such physiological loading conditions can be challenging: measuring them *in vivo* using strain gauges [6] or instrumented prostheses [7,8] are invasive methods, and other options, such as musculoskeletal models [9], require high modeling effort. Inverse bone remodeling (IBR) is another method to reconstruct the loading history from the microstructure of bones, which can be imaged using computed tomography (CT).

IBR uses information imprinted in the bone by (re)modeling to obtain physiological loads by reconstructing the loading history

* Corresponding author.
E-mail address: bachmann@ilsb.tuwien.ac.at (S. Bachmann).

https://doi.org/10.1016/j.cmpb.2023.107549

[10]. Mechanical stimuli acting on the bone will elicit an adaption of bone tissue [11]. Thus, by regular and prolonged loading of the bone, the bone will (re)model to withstand the applied loading in an optimized way [12]. IBR aims to invert this process and find the loading that caused the bone to adapt [10]. A set of probable unit load cases is applied to a finite element (FE) model of the bone to solve the inverse problem. Then, an optimization procedure finds scaling factors for the load cases, such that the combined and scaled load cases load the bone in an optimal way. For bone that is in homeostasis, i.e., that has already adapted to a certain loading condition, such an optimal loading can be found when the loading state in the bone is distributed homogeneously and close to a target value.

The first IBR implementation used 2D homogenized-FE (hFE) models to predict loading conditions at the proximal femur [13–16]. Another implementation of IBR is designed for high-resolution µFE and uses a simplified optimization criterion, as the internal bone loading can be directly evaluated at the tissue level [17]. This µFE-based IBR method was already applied, for example, to identify hip loading patterns of animals [18] or to investigate the plausibility of the predictions on human femora [19]. Recently, the method was translated to hFE [20] to speed up computational time and to be able to use sophisticated boundary conditions such as articular contact in the future.

The recently developed hFE-based IBR model was so far only applied at the distal radius [20], a bone with relatively simple geometry, homogeneous microstructure, and simple loading condition, as the bone experiences almost exclusively axial compression in a physiological scenario [21]. A study investigating the predictive power on bones with a more diverse loading regime and heterogeneous microstructure is still missing. Furthermore, only section forces have been estimated so far, while the ultimate goal would be to estimate joint loadings.

To fill this gap, hFE-based IBR could be applied to the proximal femur to predict hip joint loading. In contrast to the distal radius, the proximal femur microstructure is heterogeneous, with differently oriented trabeculae, and the outer bone geometry is more complex. Also, *in vivo* measurements from instrumented prostheses [7] are available. Thus, the results of IBR can be checked for plausibility. From a clinical point of view, the proximal femur is of interest because it poses a high fracture risk, especially in elderly people [22], and is thus also a common bone to evaluate fracture risk on [23]. Lastly, the femur is the longest and most massive bone in the human body and is thus a good test case for the computational efficiency of the hFE-based IBR method.

The primary objective of this study was to apply the previously developed hFE-based IBR algorithm to the proximal femur and assess its performance. Specifically, it should be tested if the results by Synek *et al.* [19] achieved by µFE-based IBR can be reproduced by hFE-based IBR. A secondary objective was to assess how simple the hFE models can be to still get results in good agreement with µFE-based IBR. This information is also important if image data with lower image quality or resolution, such as QCT or MRI, should be used in the future as the basis of hFE-based IBR.

2. Methods

A graphical overview of the study is given in Fig. 1. First, micro-CT (µCT) images were processed, and µFE and hFE models were created from the same µCT images. While µFE only used a single isotropic material for the entire bone, different material models were used in hFE. Unit load cases were applied in four directions in the frontal plane. After solving the FE models, optimal loading was determined using IBR. The peak and mean force of each model were then calculated, and all models were compared with respect to µFE, which acted as the baseline.

2.1. Finite element model meshes and boundary conditions

A set of 19 images of proximal femora was used from a previous study [19,24]. No additional experiments or scans were performed on the specimens. The images were originally scanned in a µCT scanner with 0.0303 mm voxel size but were resampled to 0.0606 mm voxel size to reduce computational costs. This resolution was shown to still be sufficient for µFE based IBR [25]. The femur was rotated into a head-centered coordinate system, and the head region was cropped from the femur, as described previously [19] (Fig. 1a). Following [19], a voxel-based cartilage layer was added, 2.2 mm larger than the radius of the head. The head radius was found by fitting a sphere to the femoral head. Additionally, trabecular and cortical volumes were identified using the "fill" method [26] of medtool (Version 4.6, Dr. Pahr Ingenieurs e.U., Pfaffstätten, Austria) and labeled in the images.

µFE meshes were generated in analogy to [19] by direct conversion of each voxel belonging to bone or cartilage to a hexahedral element. Smooth FE meshes were created using the "bone mesher" [26] of medtool and a custom cartilage mesh generator implemented with gmsh [27]. In brief, the algorithm generates a tetrahedral volumetric mesh of the trabecular region and uses a thickness map of the cortex to create a thin, closed cortical layer using wedge elements. The resulting mesh had a maximum element size of 2.5 mm for the trabecular elements and approximately 2.5 mm side length of the triangular basis of the cortex wedge elements. Details of mesh convergence can be found in the appendix. The cartilage layer was constructed using the same parameters as in µFE but used an additional refined loading area using a maximal element size of 1mm. The cortical bone used second-order wedge elements (C3D15), while the trabecular bone and the cartilage were meshed using second-order tetrahedrons (C3D10).

Force boundary conditions were applied in 40° spherical cap areas on the cartilage layer [19] (Fig. 1b). For µFE, a normal force vector, acting in the head center, was constructed, and the force was evenly distributed among all nodes in the contact area. For hFE, a pressure acting on the contact surface area was applied to model the same force magnitude and direction as in µFE (for assessment of the compatibility of the two boundary conditions, see the appendix). The two cut surfaces at the neck were pinned in all three directions. Four load cases were applied using -20°, 20°, 60°, and 100°, all in the frontal plane, with a unit force magnitude of $F_u = 1$ kN per load case.

2.2. Material models

An isotropic tissue material was used for the bone in the µFE models using $E = 12$ GPa and a Poisson ratio of $\nu = 0.3$ [20,28]. The cartilage was modeled with $E = 10$ MPa and $\nu = 0.3$ [19]. hFE models were created using different material mappings for the trabecular and cortical bone regions, two models with homogeneous (density-independent) and two with inhomogeneous (density-dependent) finite element material properties (Fig. 1d, Table 1). The simplest model (HOM) used the same isotropic and homogeneous material for both cortex and trabecular bone. The next model (HOM_HOM) used two different isotropic homogeneous materials for the cortex and trabecular bone. The two most

Table 1
Elastic base material properties. See the appendix for details of the material models. tb: trabecular; ctx: cortex.

Model	E_0 (MPa)	G_0 (MPa)	ν_0 (-)	k (-)	l (-)
INHOM (tb)	10905	-	0.25	2.00	-
INHOM (ctx)	12000	-	0.30	2.00	-
ORTHO (tb)	13758	4136	0.22	2.01	1.20

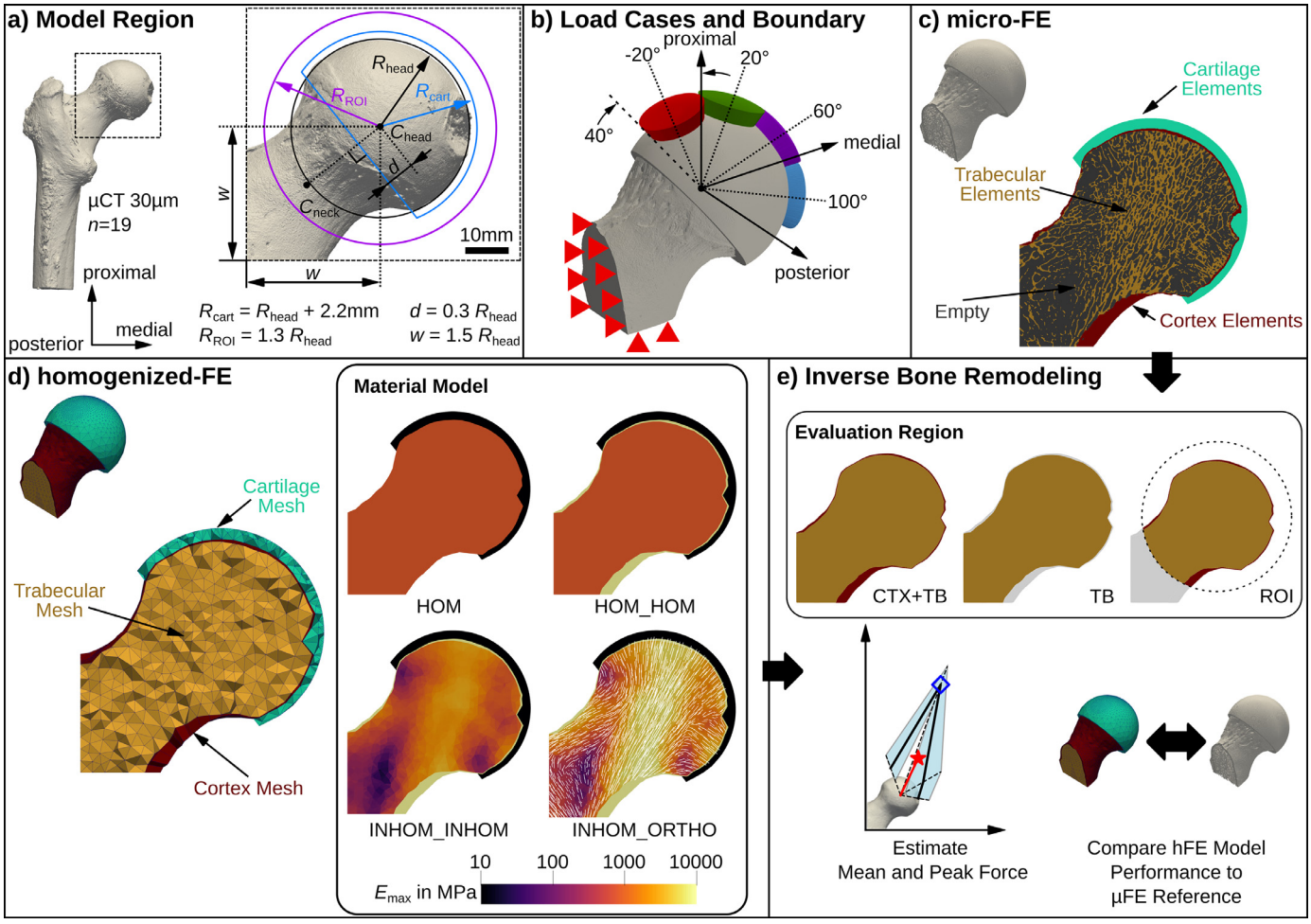

Fig. 1. Graphical overview of the study. (a) shows the selected region for the femoral head model, the anatomical landmarks and used sizes for the cartilage and region of interest (ROI). (b) gives an overview of the four applied load cases and their location on the surface of the cartilage. (c) µFE model showing different regions inside the model. The "empty" regions are not actually modelled. (d) overview of homogenized-FE (hFE) model and the four different material models used. HOM: cortex and trabecular bone use the same homogenous material. HOM_HOM: cortex and trabecular bone use a different but homogenous material. INHOM_INHOM: both cortex and trabecular bone are modeled with two density-dependent inhomogeneous materials. INHOM_ORTHO: the cortex uses an inhomogeneous material law while the trabecular bone uses an inhomogeneous orthotropic material law. (e) Inverse Bone Remodeling (IBR). Shown are the evaluation regions schematically. CTX+TB: both cortical and trabecular bone were used in the optimization. TB: only trabecular bone was used. ROI: cortical and trabecular bone inside a sphere (see definition of ROI in a) were used. With IBR, the mean and peak force was estimated and the different hFE models were compared to the reference, which was µFE.

advanced models used a density-dependent inhomogeneous cortex with either a density-dependent inhomogeneous trabecular bone (INHOM_INHOM) or a density and fabric-dependent orthotropic trabecular bone (INHOM_ORTHO).

Homogenized base material properties were taken from Panyasantisuk *et al.* [29], who used FE-based homogenization with periodicity-compatible mixed uniform boundary conditions. These values were scaled to match the 12 GPa µFE material. Two different types of material mapping models, an inhomogeneous, density-dependent material and an orthotropic, density and fabric dependent material (Zysset-Curnier material model [30]) were considered. Equations of all material models are given in the appendix. Homogeneous material properties of the HOM and HOM_HOM models were calculated by using the average density and inserting it into an inhomogeneous material mapping law. For the HOM model, the average density (31.9%) of the entire modelled region was used and inserted in the "INHOM (tb)" law (Table 1) and yielded an elastic modulus of $E = 1108$ MPa. For HOM_HOM, the average density for trabecular (25.7%) and cortical bone (97.3%) was evaluated separately and yielded elastic moduli of $E = 720$ MPa using the "INHOM (tb)" law and $E = 11361$ MPa by using the "INHOM (ctx)" law, respectively. The inhomogeneous cortex model used the same inhomogeneous model as the trabecular bone but a tissue modulus of $E_0 = 12$ GPa and Poisson ratio $\nu = 0.3$ was used, such that it matches µFE at 100% bone density. The cartilage was modeled using $E = 10$ MPa and $\nu = 0.3$, same as in µFE [19].

To map the inhomogeneous isotropic and orthotropic material to the meshes, a material mapping algorithm [31] in medtool was used (Sampling sphere diameter: 5 mm, background grid distance: 2.5 mm) using the segmented high-resolution image data, computing local density and fabric and using the corresponding material mapping law to get the element-wise elastic material properties.

2.3. Inverse bone remodeling

An hFE-based IBR algorithm was implemented as presented previously [20], which is a general extension of the µFE-based IBR of Christen *et al.* [17]. In brief, the algorithm scales the applied load cases using scaling factors α_i such that the difference between the accumulated SED in the bone and a set target stimulus $\tilde{U}_0$ is minimized. The hFE-based IBR algorithm uses a power-law function based on density to scale the tissue-level quantities to the continuum-level. The optimization function can be written as the

minimization of a residual function:

$$\min_{\alpha_i \in \mathbb{R}_0^+} r(\alpha_i) = \sum_{j=1}^{N_{IP}} \left(\tilde{U}_0 \ \rho_j^d - \frac{1}{N_{LC}} \sum_{i=1}^{N_{LC}} \alpha_i^2 \ U_{j,i} \right)^2 V_j$$

For all N_{IP} integration points in the FE mesh and N_{LC} unit load cases. V_j denotes the volume, and ρ_j the density of the integration point j. $U_{j,i}$ is the SED in integration point j for load case i. The exponent d, required in the power-law, was identified in analogy to a previous study [20] and was found to be $d = 1.297$. Details on the parameter identification can be found in the appendix. The target tissue stimulus was fixed to $\tilde{U}_0 = 0.02$ MPa [17,19]. The hFE models used full-integration for all elements and the density in each element was assumed to be constant. Field values in µFE were only evaluated at the centroids and the density of each element was assumed to be 100%.

IBR was then performed on three sets of elements. First, the full FE models were used, including both cortical and trabecular bone [19]. Second, only the trabecular elements were considered in the optimization to avoid bias from the cortical elements [32]. Third, a region of interest (ROI) was cropped from the head, using a spherical region with a radius of 1.3 R_{head} (see Fig. 1a), following the hypothesis that sufficient information regarding the joint load direction is "stored" in the head region. For the ROI evaluation, both trabecular and cortical bone was used in the optimization.

2.4. Evaluation of models

The computational performance was measured as total CPU-time for the solving of the FE models. To qualitatively compare the overall predictive performance between µFE and hFE, the loading history was visualized. The loading history is represented by a set of scaled load resultant forces $\alpha_i \boldsymbol{F}_i$ [19]. As each of the load cases has the same unit load magnitude F_u, the loading history can also be written as a vector of the scaling factors: $F_u[\alpha_1, \alpha_2, \alpha_3, \alpha_4]^T$. To quantify the error between hFE-based IBR and µFE-based IBR, the root mean squared error (RMSE) between the loading history vectors was evaluated.

For further interpretation of the predicted forces, the peak and mean force were calculated from the loading history. The peak force $\boldsymbol{F}_{peak} = \alpha_i \boldsymbol{F}_i$ was defined as the force with the highest scaling factor α_i and the mean force was calculated as $\boldsymbol{F}_{mean} = 1/4 \sum_{i=1}^{4} \alpha_i \boldsymbol{F}_i$. The magnitude $|\boldsymbol{F}|$ and angle ϕ were calculated for both peak and mean force vectors to analyze them separately. To have an error measure relative to the peak force, the RMSE was standardized by the respective µFE peak force magnitude. This measure is then referred to as RMSE%.

2.5. Hardware and software

All µFE models were solved in ParOSol [33] on a dual Intel(R) Xeon(R) Gold 6144 with a base frequency of 3.5 GHz using 16 processes in parallel. The hFE models were solved in Abaqus V6R2022 (Dassault Systèmes, Vélizy-Villacoublay, France) on an Intel(R) Xeon(R) CPU E3-1231 v3 with a base frequency of 3.4 GHz using four processes in parallel. IBR, pre- and post-processing was performed in Python 3.7.4 (Python Software Foundation, https://www.python.org), scipy 1.7.2 [34] and medtool 4.6 (Dr. Pahr Ingenieurs e.U., Pfaffstätten, Austria, http://www.medtool.at).

3. Results

3.1. Computational performance

The overall FE solving time, measured as total CPU-time, was reduced by 4 to 5 orders of magnitude using hFE instead of µFE models from an average of 500 h to under 60 s (Table 2). The homogeneous hFE models (HOM and HOM_HOM) were solved approximately twice as fast as inhomogeneous/orthotropic hFE models. Number of degrees of freedom ranged from 354 million to 598 million in µFE, and from 110 thousand to 177 thousand in hFE.

Table 2
Average total CPU time required for solving all load cases of the FE models. HOM, HOM_HOM, INHOM_INHOM, and INHOM_ORTHO denote the hFE models with different material modeling strategies.

	Mean	SD	Min	Max
µFE	499.9 h	387.2 h	185.8 h	1841.7 h
INHOM_ORTHO	47.0 s	8.1 s	32.3 s	63.4 s
INHOM_INHOM	49.2 s	8.1 s	35.6 s	63.0 s
HOM_HOM	22.3 s	4.6 s	14.9 s	31.3 s
HOM	23.3 s	4.3 s	16.7 s	31.1 s

Table 3
RMSE% of the loading history (RMSE divided by µFE peak force) for all models and evaluation regions. Values are given in percent as mean ± std. CTX+TB: full evaluation region. TB: only trabecular bone considered in evaluation. ROI: region of interest for evaluation.

	CTX + TB	TB	ROI
INHOM_ORTHO	18.49 ± 4.32	12.08 ± 2.97	14.16 ± 2.45
INHOM_INHOM	17.54 ± 3.87	13.62 ± 2.58	14.91 ± 4.08
HOM_HOM	29.08 ± 4.73	38.83 ± 5.98	32.27 ± 4.44
HOM	42.95 ± 5.81	39.03 ± 6.56	40.81 ± 5.54

3.2. Loading history

The optimally scaled forces obtained from IBR were influenced by the type of material model used. In general, more information in the model (density, fabric) led to a better agreement with the µFE results (Fig. 2). The pattern of the individual loading history (α_1 to α_4) were strongly dependent on the material model. While INHOM_ORTHO and INHOM_INHOM showed a similar pattern to µFE, HOM_HOM and HOM showed a different pattern (Fig. 2). In HOM, the 20° and 60° load cases were upscaled strongly and in HOM_HOM almost a uniform load distribution was predicted between the four load cases. A detailed box-plot comparing all four scaling factors separately, as well as Bland-Altman plots of the scaling factors can be found in the supplemental material.

The RMSE of the loading history (Fig. 3) and the standardized RMSE% (Table 3) quantitatively confirmed the trend that more information in the model (density, fabric) improved the prediction. INHOM_ORTHO and INHOM_INHOM gave the lowest errors, indicating the best agreement with the µFE results. Using different evaluation regions showed a similar trend between the different models, but INHOM_ORTHO and INHOM_INHOM achieved overall lower errors when the trabecular evaluation region was used.

While different hFE material models resulted in large differences in the predicted loading histories, the evaluation region of the IBR model only led to minor differences (Figs. 2 and 4). Using trabecular or ROI evaluation regions led to a more similar pattern between µFE-based IBR and hFE-based IBR with the INHOM_INHOM and INHOM_ORTHO models. Specifically, the 60° load case was downscaled and -20° and 20° load cases were upscaled when using trabecular or ROI region instead of the full evaluation region.

3.3. Peak and mean force

Averaged peak and mean forces are shown in Fig. 2, while Fig. 4 presents magnitudes and angles separately.

The magnitude of the mean force was in a similar range to µFE for INHOM_INHOM, overestimated for INHOM_ORTHO, and under-

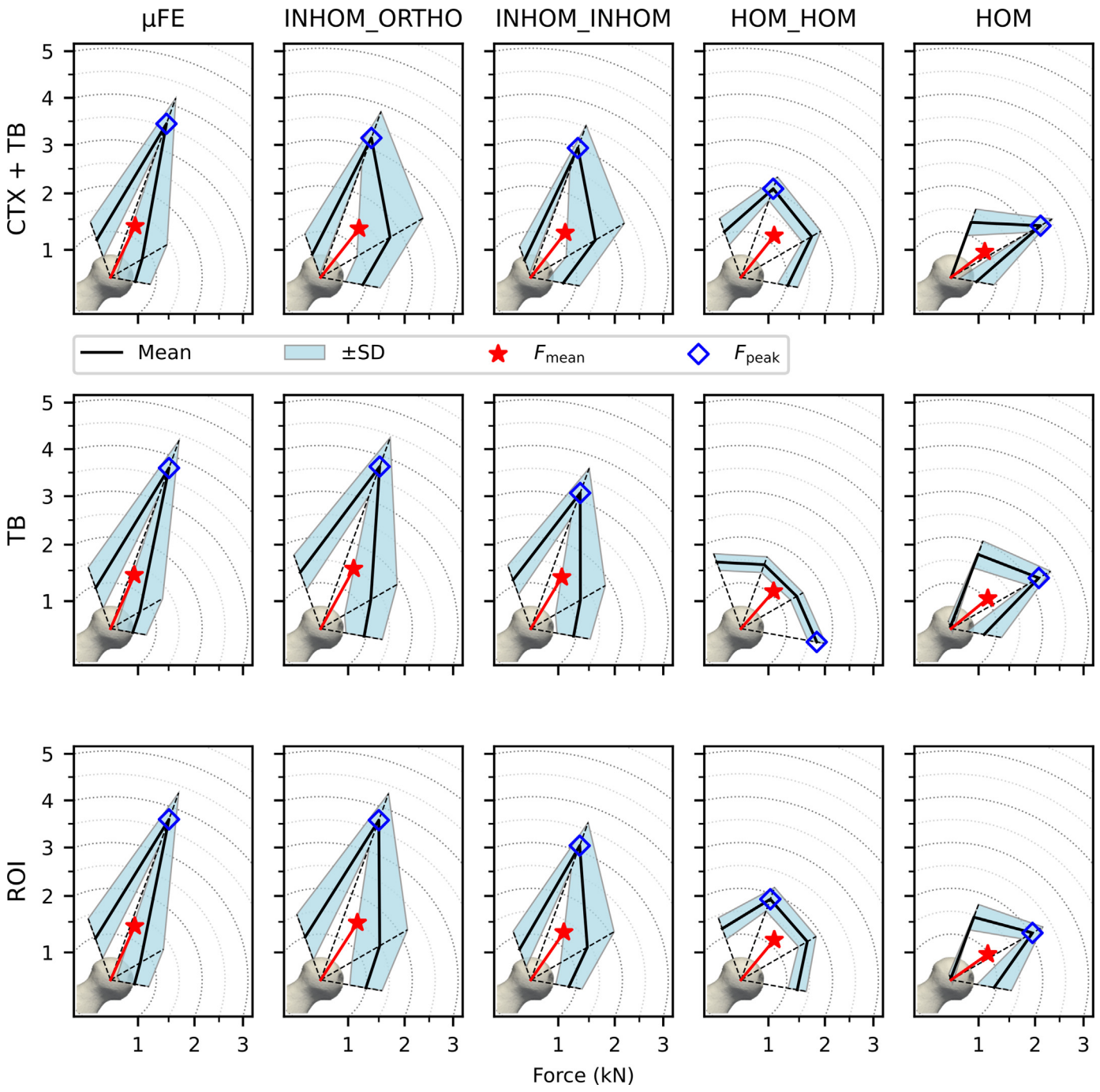

Fig. 2. Polar plots of the predicted loading history (mean and ±standard deviation), mean force, and peak forces for the different material models (one per column) and different optimization regions (one per row). The isolines of the polar plot show the force magnitude, the dashed lines give the four loading directions (-20°, 20°, 60°, and 100°).

estimated for both HOM and HOM_HOM (Fig. 4a). The angle of the mean force was consistently tilted towards the 60° load case using hFE-based IBR (Fig. 4b). This was particularly pronounced in the HOM model, where the mean force pointed almost entirely in the 60° load case direction.

The peak force magnitude was systematically underestimated by hFE-based IBR in the HOM, HOM_HOM, and INHOM_INHOM models, whereas good agreement with µFE-based IBR was found using INHOM_ORTHO model (Fig. 4c). The predicted peak force angle (Fig. 4d) was correctly identified in almost all samples using the INHOM_INHOM and INHOM_ORTHO models. The HOM_HOM model identified the peak force angle for most samples correctly using the full and ROI evaluation region but not when using the trabecular evaluation region, where a peak force angle of 100° was predicted in all samples. The HOM model failed to predict the peak force angle, as 60° was predicted for almost all samples and in all three evaluation regions.

The resulting peak and mean forces were less affected by the optimization region than the material models. A notable difference, however, was the erroneous peak force direction for the HOM_HOM models and the trabecular evaluation region in all 19 samples, which was predicted correctly for 16 samples using the entire evaluation region and 14 samples using the ROI evaluation region.

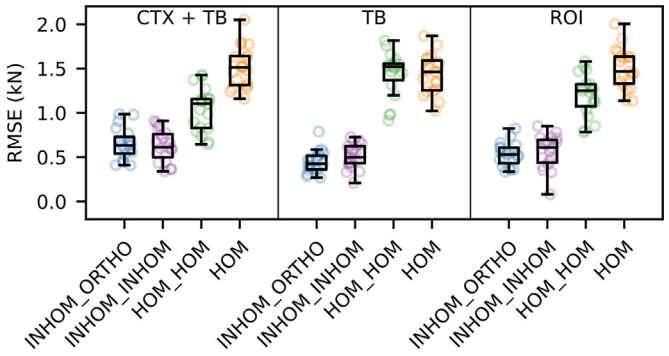

Fig. 3. Root mean squared error (RMSE) of the loading history vector ($F_u\ [\alpha_1,\alpha_2,\alpha_3,\alpha_4]^T$) between µFE and the respective hFE model for each evaluation region.

4. Discussion

This study showed that hFE-based IBR can be used to predict the loading history, in terms of scaling factors, mean, and peak hip joint forces at the femoral head. With the best hFE models, hFE-based IBR predictions were in good agreement with µFE-based IBR and offered a huge computational speed gain due to the lower number of elements. Using an inhomogeneous rather than homogeneous trabecular bone material model had the highest influence on the predicted values, whereas the evaluation region of the IBR algorithm generally had a minor influence on the results.

Using different types of material models gave a clear indication of the primary information of the bone structure used in the IBR algorithm. The fully homogeneous model (HOM) represents the "purely geometrical" information. Using the HOM models, IBR led to a strong overestimation of the load in the direction of the femoral neck, which is the stiffest direction if the cortical thickness and bone density distribution are neglected. When the distinction between cortical and trabecular bone was added in the HOM_HOM model, the influence of the geometry decreased and resulted in the prediction of almost uniform loading of the femoral head. As soon as inhomogeneous bone material was used in the hFE models, either with or without orthotropy, the IBR predictions came close to the predictions of µFE. A reason could be the principal compressive group of the femoral microstructure [35], which is only represented in the inhomogeneous models and is responsible for the higher scaling of the 20° load case in comparison to the HOM and HOM_HOM models. In this case, the orthotropic material scales the stiffnesses in the principal direction of the compressive group even higher and thus gives an even better prediction than the inhomogeneous material. However, the 60° and 100° load cases were consistently scaled higher using hFE when compared to µFE. One reason might be a too stiff trabecular material behavior resulting from the material mapping, which computed the bone densities based on several sampling spheres with a diameter of 5 mm. This might lead to the inability to resolve small low-density regions or steep density gradients, such as behind the fovea capitis. However, for a material that also depends on orientation, the sampling sphere cannot be chosen arbitrarily small [31,36]. To ensure comparability between the INHOM and ORTHO models, the sampling sphere was used with the same size in both models.

The bias of hFE-based IBR due to material models also influenced the agreement of the mean and peak force with µFE-based

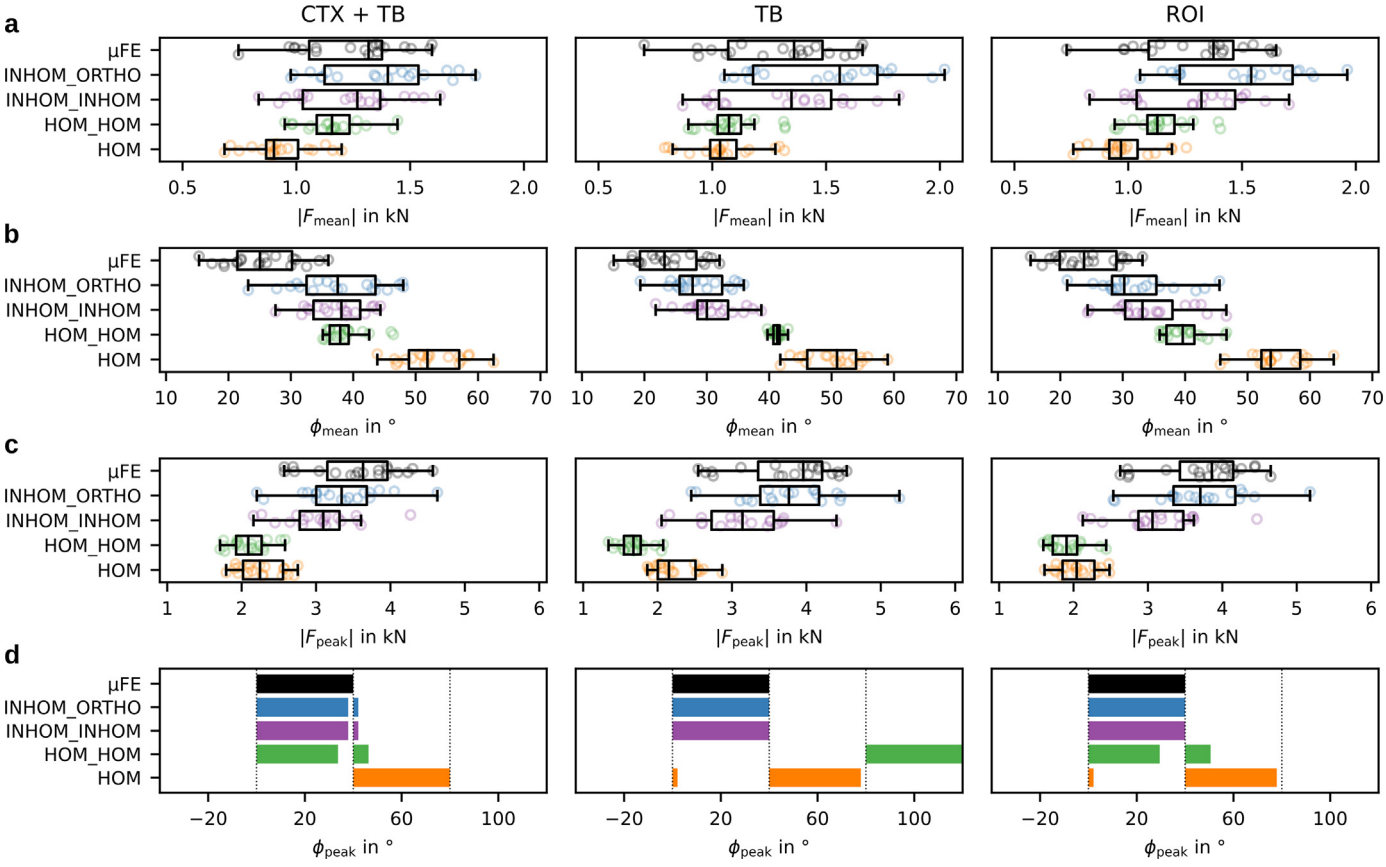

Fig. 4. Matrix of force results: Three evaluation regions CTX+TB, TB, ROI versus different force measures. (a) Mean force magnitude. (b) Mean force angle. (c) Peak force magnitude. (d) Peak force angle. The bar for each of the four discrete angles gives the percentage of models predicting that angle as peak. For instance, the HOM_HOM model for the TB evaluation region predicted 100% of the samples to be 100° but 74% to be 20° and 16% to be 60° for the ROI evaluation region.

IBR. While the mean force magnitude was least influenced by the kind of hFE model, the mean force angle was strongly influenced due to the higher scaled 60° and 100° load cases. On the other hand, the peak force angle was correctly predicted for most models and evaluation regions (over 73% for HOM_HOM, except for TB region; over 94% for INHOM_INHOM and INHOM_ORTHO, independent of region), but the peak magnitude varied largely. The mean force magnitude is a more robust measure, as it averages all scaling factors, while the peak force only uses a single scale factor [19]. Conversely, the peak force angle is more robust than the mean force angle. That is, because the proportions of the scaling factors to each other influence the mean force angle, while the maximum scale factor is found reliably, if at least inhomogeneous material is used.

Using different evaluation regions in IBR led to no drastic change in the joint force predictions, except for the HOM_HOM model. In this case, the predicted peak force angle changed when the trabecular evaluation region was used. µFE-based predictions were generally less influenced by the evaluation region than hFE-based predictions. Thus, selecting a region might be more important in hFE than in µFE, to filter for example, very high SEDs in regions where the boundary conditions are applied.

The results of this study suggest that for the application of hFE-based IBR in the future, at least inhomogeneous material properties are required. Only modeling the pure geometry or cortical and trabecular volumes with constant density increased the error in the prediction 2 to 3 times. Further, models that did not include material inhomogeneity (HOM, HOM_HOM) were not able to predict the peak force angle in a robust manner. The added orthotropy only influenced the results slightly in this study. However, the optimization criterion applied in this study does not use the orthotropy information and a different optimization function could yield better results together with the orthotropic model. Such an optimization function can be found, for example, by fitting the required parameters on trabecular bone cubes with optimized loading conditions determined using µFE-based IBR, in as asuggested in [20]. While there is an additional gain in speed when using homogeneous models (HOM and HOM_HOM) instead of inhomogeneous models (INHOM_INHOM and INHOM_ORTHO), the speed gain between different hFE models was marginal (30 versus 60 CPU seconds) when compared to the gain of hFE versus µFE in general (500 CPU hours). Given the high gain in computational speed and minor drawbacks in terms of accuracy, this study suggests that hFE-based IBR might also be suitable for load predictions using clinical imaging technology. In future, inhomogeneous models could be created from clinical CT scans [14,15] which were shown to predict strength equally well as inhomogeneous models created from high resolution CT-scans [37]. However, the results of IBR with hFE models created from clinical CT scans remain to be evaluated in detail.

This study has some limitations. Only simplified boundary conditions with uniform pressure distributions were used, as circular contact patches with resultant forces only in the frontal plane were used. However, in reality peak force components are also acting in the sagittal and transversal plane in the hip [7], which cannot be identified with the current set of load cases. The restriction of load cases was necessary to enable a comparison of the results between hFE and µFE-based IBR with feasible runtimes. Also, the pinning of the cut-planes at the neck is a simplification of the physiological boundary. While using an ellipsoidal load distribution instead of the here applied uniform pressure had only a small influence on the results when using µFE-based IBR [19], a contact boundary condition might also give more realistic stress distributions [38] and thus also more realistic results in IBR. In addition, only the femoral head was considered for IBR, but muscle forces on the proximal femur might influence the result. Muscle forces were so far only modeled in 2D representations of the proximal femur in IBR [13–16] and in 3D using neural network based IBR [39]. However, the effect of muscle forces on IBR is not yet known and might be negligible, as the stress distribution of the head is not influenced by adding muscle forces [40]. Thus, further studies are required to elucidate the effect of different boundary conditions on IBR. Finally, the continuum target stimulus of the IBR algorithm used here only contains density information. Orientation of the material could be added in the future to further improve the joint load predictions. The cartilage was modelled as an elastic material with Poisson's ratio $\nu = 0.3$ both in µFE and hFE. However, cartilage is typically modelled as incompressible with Poisson's ratios near 0.5. The reason for the lower Poisson's ratio in this study was to ensure comparability with µFE, as the µFE solver ParOSol only allows for a single Poisson's ratio for the whole model [33]. Using a Poisson's ratio of $\nu = 0.495$ and hybrid elements (C3D10H) resulted in slightly changed scaling factors in the hFE models (see Supplemental material for correlation plot) but did not change the main conclusions of this study. Finally, the here reported CPU-times for µFE and hFE were collected on two different types of CPUs and different number of parallel processes as well as different FE solvers. A high number of parallel processes is required for µFE to allow for feasible runtimes. However, this leads to systematic differences between the reported CPU-times. Therefore, the CPU-times given are only comparable to a limited extent and should not be interpreted as a true benchmark, but still give a reasonable estimate if µFE and hFE were run on the same hardware.

To conclude, hFE-based IBR allows the prediction of hip joint loading based on a CT scan of the femoral head, but with much lower runtime compared to µFE-based IBR. The accuracy of the predictions depended on the used material models and at least inhomogeneous material properties were required to get to similar results to µFE-based IBR. The evaluation region used for optimization only had minor influence on the result. These results indicate that *in vivo* load prediction using IBR based on clinical CT data may be feasible in the future.

Declaration of Competing Interest

Dieter H. Pahr is CEO of Dr. Pahr Ingenieurs e.U., which develops and distributes Medtool. All other authors declare no competing interests.

Acknowledgements

This research has received funding from the European Research Council (ERC) under the European Union's Horizon 2020 research and innovation program (Grant Agreement No. 819960).

The authors acknowledge TU Wien Bibliothek for financial support through its Open Access Funding Programme.

Appendix

A. Homogenized material models

The here used material models were either a density dependent power-law model or a density and fabric dependent Zysset-Curnier [30] type model. While the power-law yields an isotropic model (two independent material parameters), the Zysset-Curnier model is orthotropic (nine independent material parameters).

The power-law uses three parameters: The base elastic-modulus E_0, the base Poisson number ν_0, and the density exponent k. The following equation is used to get the density dependent elastic-modulus:

$$E = E_0 \ \rho^k \tag{1}$$

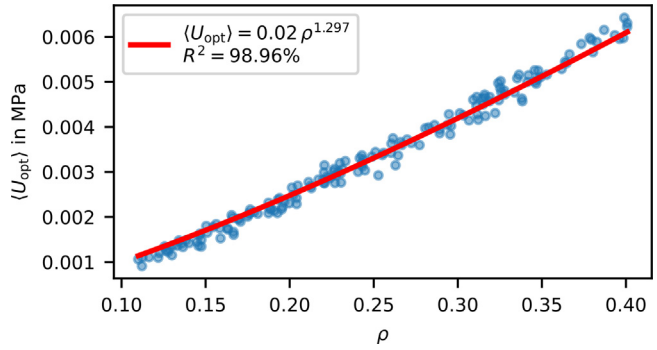

Fig. 5. Curve fitting of the power-law exponent d for the continuum optimization function.

The Zysset-Curnier model uses, additionally to the density, the three eigenvalues m_i of the fabric tensor, which is a measure for the orientation of the microstructure. The fabric tensor has to be scaled such that the trace of the tensor is equal to 3. An additional exponent l is used to scale the eigenvalues. There are now three elastic-moduli:

$$E_i = E_0\ \rho^k\ m_i^{2l} \tag{2}$$

As well as three independent shear moduli:

$$G_{ij} = G_0\ \rho^k\ \left(m_i\ m_j\right)^l \tag{3}$$

And three independent Poisson numbers:

$$\nu_{ij} = \nu_0 \left(\frac{m_j}{m_i}\right)^l \tag{4}$$

In the case of an isotropic material, where all eigenvalues are 1, the model reduces to the power-law model (Eq. (1)), if the following Eq. (5) is fulfilled for ν_0:

$$\nu_0 = \frac{E_0}{2G_0} - 1 \tag{5}$$

Parameter identification

Parameters of the hFE-based IBR algorithm were identified in analogy to [20]. To identify the power-law exponent d of the optimization function, the same set of 167 trabecular bone cubes as were already used for the identification of the homogenized elastic material properties [29] were uses. Six canonical load cases, using periodicity compatible mixed uniform boundary conditions (PMUBC), were applied to the cubes. Then, the optimized loading state was found by applying IBR to the six load cases. Afterwards, the accumulated macroscopic SED $\langle U_{opt} \rangle$ was calculated and fitted for the relative density ρ of each of the cubes using curve fitting (Fig. 5). In the curve fitting process, the variable $\tilde{U}_0$ was fixed to 0.02 MPa.

Agreement of hFE and µFE boundary conditions

To validate that the used boundary conditions in µFE and hFE give the same results, models of a single femoral head were created using the finest mesh resolution in hFE (see Mesh Convergence). The model was completely filled with an isotropic homogeneous material and the force (µFE) and pressure (hFE) boundary conditions were applied for the 20° load case. The reaction force at the neck boundary was calculated for both models, to compare the error using the different loadings. The magnitude was 1000.1 N for µFE and 996.4 N for hFE. Then, the displacement field of the two models was compared on each node of the hFE mesh by searching for the nearest node in the µFE mesh. A corresponding µFE node was found on average in 0.029 mm ± 0.009 mm distance and the displacement field differed on average by a magnitude of 0.012 mm ± 0.006 mm with an average displacement magnitude of 0.239 mm ± 0.135 mm for µFE and 0.233 mm ± 0.135 mm for hFE. The main difference between the two meshes was the underestimation of volume in the neck region in the hFE mesh due to large pores in the cortex, thus giving a softer model with slightly larger displacements in the head. Given that the actual reaction force magnitude only differed by less than 1% and the displacement differences can be explained by the lower hFE mesh volume, the boundary conditions were assumed to be comparable.

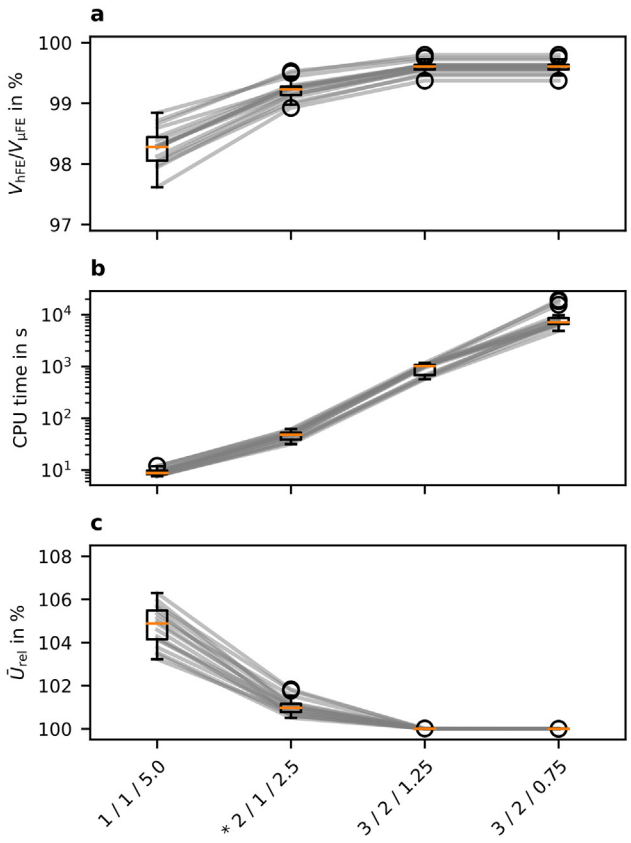

Fig. 6. Mesh convergence study. (a) Change in volume, relative to the true volume measured in the CT image. (b) total CPU time for solving the model (all four load cases). (c) change of mean SED $\tilde{U}$, relative to the finest model (3 / 2 / 0.75) for the 20° load case. Asterisk (*) marks the selected model.

Mesh convergence

To test the dependency of element size in the hFE meshes, different mesh densities were created and the INHOM_ORTHO model was applied for 17 of the 19 femora. Two models were removed because the cartilage mesh was not created correctly for the coarsest mesh. The volume weighted mean SED was calculated for each of the models and standardized by the finest model. Fig. 6 gives the mean SED for the 20° load case, the total runtime of each model and bone volume (trabecular and cortical volume, not including the cartilage layer). The name of each model is the number of cortical refinement steps, the number of elements over the cortex thickness and the maximal element size for the trabecular bone. Finally, the model 2/1/2.5 (2 refinement steps, 1 element over the cortex, 2.5 mm maximal element size) was selected, as the deviation of mean SED from the finest model was on average below 5% and it had runtimes one order of magnitude lower than the next finer model.

The volumes of the hFE meshes with the selected meshing parameters were compared to the voxel-based volume of µFE, to ensure that both models are not biased because of different volumes. The hFE meshes had 0.5% to 1.1% less volume than µFE, due to the smoothing of the mesh surfaces in hFE.

Supplementary materials

Supplementary material associated with this article can be found, in the online version, at doi:10.1016/j.cmpb.2023.107549.

References

[1] F. Taddei, I. Palmadori, W.R. Taylor, M.O. Heller, B. Bordini, A. Toni, E. Schileo, European Society of Biomechanics S.M. Perren Award 2014: Safety factor of the proximal femur during gait: a population-based finite element study, J. Biomech. 47 (2014) 3433–3440, doi:10.1016/j.jbiomech.2014.08.030.

[2] G. Bergmann, F. Graichen, A. Rohlmann, A. Bender, B. Heinlein, G.N. Duda, M.O. Heller, M.M. Morlock, Realistic loads for testing hip implants, Biomed. Mater. Eng. 20 (2010) 65–75, doi:10.3233/BME-2010-0616.

[3] C. Ruff, B. Holt, E. Trinkaus, Who's afraid of the big bad Wolff?: "Wolff's law" and bone functional adaptation, Am. J. Phys. Anthropol. 129 (2006) 484–498, doi:10.1002/ajpa.20371.

[4] P. Pankaj, Patient-specific modelling of bone and bone-implant systems: the challenges, Int. J. Numer. Methods Biomed. Eng. 29 (2013) 233–249, doi:10.1002/cnm.2536.

[5] L. Berger, D. Pahr, A. Synek, Articular contact vs. embedding: Effect of simplified boundary conditions on the stress distribution in the distal radius and volar plate implant loading, J. Biomech. 143 (2022) 111279, doi:10.1016/j.jbiomech.2022.111279.

[6] R.A. Nazer, J. Lanovaz, C. Kawalilak, J.D. Johnston, S. Kontulainen, Direct *in vivo* strain measurements in human bone-a systematic literature review, J. Biomech. 45 (2012) 27–40, doi:10.1016/j.jbiomech.2011.08.004.

[7] G. Bergmann, A. Bender, J. Dymke, G. Duda, P. Damm, Standardized loads acting in hip implants, PLoS ONE 11 (2016) e0155612, doi:10.1371/journal.pone.0155612.

[8] G. Bergmann, A. Bender, F. Graichen, J. Dymke, A. Rohlmann, A. Trepczynski, M.O. Heller, I. Kutzner, Standardized loads acting in knee implants, PLoS ONE 9 (2014) e86035, doi:10.1371/journal.pone.0086035.

[9] A. Erdemir, S. McLean, W. Herzog, A.J. van den Bogert, Model-based estimation of muscle forces exerted during movements, Clin. Biomech. 22 (2007) 131–154, doi:10.1016/j.clinbiomech.2006.09.005.

[10] A.A. Zadpoor, Open forward and inverse problems in theoretical modeling of bone tissue adaptation, J. Mech. Behav. Biomed. Mater. 27 (2013) 249–261, doi:10.1016/j.jmbbm.2013.05.017.

[11] H.M. Frost, Bone's mechanostat: a 2003 update, Anat. Rec. 275A (2003) 1081–1101, doi:10.1002/ar.a.10119.

[12] M.M. Barak, D.E. Lieberman, J.J. Hublin, A Wolff in sheep's clothing: trabecular bone adaptation in response to changes in joint loading orientation, Bone 49 (2011) 1141–1151, doi:10.1016/j.bone.2011.08.020.

[13] K.J. Fischer, C.R. Jacobs, M.E. Levenston, D.D. Cody, D.R. Carters, Proximal femoral density patterns are consistent with bicentric joint loads, Comput. Methods Biomech. Biomed. Eng. 2 (1999) 271–283, doi:10.1080/10255849908907992.

[14] M.A. Bona, L.D. Martin, K.J. Fischer, A contact algorithm for density-based load estimation, J. Biomech. 39 (2006) 636–644, doi:10.1016/j.jbiomech.2005.01.006.

[15] K.J. Fischer, C.R. Jacobs, M.E. Levenston, D.D. Cody, D.R. Carter, Bone load estimation for the proximal femur using single energy quantitative CT data, Comput. Methods Biomech. Biomed. Eng. 1 (1998) 233–245, doi:10.1080/01495739808936704.

[16] K.J. Fischer, F. Eckstein, C. Becker, Density-based load estimation predicts altered femoral load directions for Coxa Vara And Coxa Valga, Journal Musculoskeletal Research 03 (1999) 83–92, doi:10.1142/s0218957799000105.

[17] P. Christen, B. van Rietbergen, F.M. Lambers, R. Müller, K. Ito, Bone morphology allows estimation of loading history in a murine model of bone adaptation, Biomech. Model. Mechanobiol. 11 (2011) 483–492, doi:10.1007/s10237-011-0327-x.

[18] P. Christen, K. Ito, F. Galis, B. van Rietbergen, Determination of hip-joint loading patterns of living and extinct mammals using an inverse Wolff's law approach, Biomech. Model. Mechanobiol. 14 (2014) 427–432, doi:10.1007/s10237-014-0602-8.

[19] A. Synek, D.H. Pahr, Plausibility and parameter sensitivity of micro-finite element-based joint load prediction at the proximal femur, Biomech. Model. Mechanobiol. 17 (2017) 843–852, doi:10.1007/s10237-017-0996-1.

[20] S. Bachmann, D.H. Pahr, A. Synek, A density-dependent target stimulus for inverse bone (re)modeling with homogenized finite element models, Ann. Biomed. Eng. (2022), doi:10.1007/s10439-022-03104-x.

[21] J.M. Smith, F.W. Werner, B.J. Harley, Forces in the distal radius during a pushup or active wrist motions, J. Hand Surg. 43 (2018) 806–811, doi:10.1016/j.jhsa.2018.05.020.

[22] C.M. Court-Brown, B. Caesar, Epidemiology of adult fractures: a review, Injury 37 (2006) 691–697, doi:10.1016/j.injury.2006.04.130.

[23] J.A. Kanis, Diagnosis of osteoporosis and assessment of fracture risk, Lancet 359 (2002) 1929–1936, doi:10.1016/s0140-6736(02)08761-5.

[24] G. Iori, F. Heyer, V. Kilappa, C. Wyers, P. Varga, J. Schneider, M. Gräsel, R. Wendlandt, R. Barkmann, J.P. van den Bergh, K. Raum, BMD-based assessment of local porosity in human femoral cortical bone, Bone 114 (2018) 50–61, doi:10.1016/j.bone.2018.05.028.

[25] P. Christen, F.A. Schulte, A. Zwahlen, B. van Rietbergen, S. Boutroy, L.J. Melton, S. Amin, S. Khosla, J. Goldhahn, R. Müller, Voxel size dependency, reproducibility and sensitivity of an *in vivo* bone loading estimation algorithm, J. R. Soc. Interface 13 (2016) 20150991, doi:10.1098/rsif.2015.0991.

[26] D.H. Pahr, P.K. Zysset, From high-resolution CT data to finite element models: development of an integrated modular framework, Comput. Methods Biomech. Biomed. Eng. 12 (2009) 45–57, doi:10.1080/10255840802144105.

[27] C. Geuzaine, J.F. Remacle, Gmsh: a 3-D finite element mesh generator with built-in pre- and post-processing facilities, Int. J. Numer. Methods Eng. 79 (2009) 1309–1331, doi:10.1002/nme.2579.

[28] T. Gross, D.H. Pahr, P.K. Zysset, Morphology–elasticity relationships using decreasing fabric information of human trabecular bone from three major anatomical locations, Biomech. Model. Mechanobiol. 12 (2012) 793–800, doi:10.1007/s10237-012-0443-2.

[29] J. Panyasantisuk, D.H. Pahr, T. Gross, P.K. Zysset, Comparison of mixed and kinematic uniform boundary conditions in homogenized elasticity of femoral trabecular bone using microfinite element analyses, J. Biomech. Eng. 137 (2015), doi:10.1115/1.4028968.

[30] P.K. Zysset, A. Curnier, An alternative model for anisotropic elasticity based on fabric tensors, Mech. Mater. 21 (1995) 243–250, doi:10.1016/0167-6636(95)00018-6.

[31] D.H. Pahr, P.K. Zysset, A comparison of enhanced continuum FE with micro FE models of human vertebral bodies, J. Biomech. 42 (2009) 455–462, doi:10.1016/j.jbiomech.2008.11.028.

[32] A. Synek, C.J. Dunmore, T.L. Kivell, M.M. Skinner, D.H. Pahr, Inverse remodelling algorithm identifies habitual manual activities of primates based on metacarpal bone architecture, Biomech. Model. Mechanobiol. 18 (2018) 399–410, doi:10.1007/s10237-018-1091-y.

[33] C. Flaig, P. Arbenz, A scalable memory efficient multigrid solver for micro-finite element analyses based on CT images, Parallel Comput. 37 (2011) 846–854, doi:10.1016/j.parco.2011.08.001.

[34] P. Virtanen, R. Gommers, T.E. Oliphant, M. Haberland, T. Reddy, D. Cournapeau, E. Burovski, P. Peterson, W. Weckesser, J. Bright, S.J. van der Walt, M. Brett, J. Wilson, K.J. Millman, N. Mayorov, A.R.J. Nelson, E. Jones, R. Kern, E. Larson, C.J. Carey, İlhan Polat, Y. Feng, E.W. Moore, J. VanderPlas, D. Laxalde, J. Perktold, R. Cimrman, I. Henriksen, E.A. Quintero, C.R. Harris, A.M. Archibald, A.H. Ribeiro, F. Pedregosa, P. van Mulbregt, SciPy 1.0 Contributors, SciPy 1.0: fundamental algorithms for scientific computing in python, Nat. Methods 17 (2020) 261–272, doi:10.1038/s41592-019-0686-2.

[35] R. Kerr, D. Resnick, D.J. Sartoris, S. Kursunoglu, C. Pineda, P. Haghighi, G. Greenway, J. Guerra, Computerized tomography of proximal femoral trabecular patterns, J. Orthop. Res. 4 (1986) 45–56, doi:10.1002/jor.1100040106.

[36] D.H. Pahr, P.K. Zysset, Influence of boundary conditions on computed apparent elastic properties of cancellous bone, Biomech. Model. Mechanobiol. 7 (2007) 463–476, doi:10.1007/s10237-007-0109-7.

[37] B. Luisier, E. Dall'Ara, D.H. Pahr, Orthotropic HR-pQCT-based FE models improve strength predictions for stance but not for side-way fall loading compared to isotropic QCT-based FE models of human femurs, J. Mech. Behav. Biomed. Mater. 32 (2014) 287–299, doi:10.1016/j.jmbbm.2014.01.006.

[38] P. Yang, T.Y. Lin, J.L. Xu, H.Y. Zeng, D. Chen, B.L. Xiong, F.X. Pang, Z.Q. Chen, W. He, Q.S. Wei, Q.W. Zhang, Finite element modeling of proximal femur with quantifiable weight-bearing area in standing position, J. Orthop. Surg. Res. 15 (2020) 384, doi:10.1186/s13018-020-01927-9.

[39] N. Garijo, J. Martıńez, J.M. Garcıá-Aznar, M.A. Pérez, Computational evaluation of different numerical tools for the prediction of proximal femur loads from bone morphology, Comput. Methods Appl. Mech. Eng. 268 (2014) 437–450, doi:10.1016/j.cma.2013.10.005.

[40] L. Cristofolini, M. Juszczyk, S. Martelli, F. Taddei, M. Viceconti, *In vitro* replication of spontaneous fractures of the proximal human femur, J. Biomech. 40 (2007) 2837–2845, doi:10.1016/j.jbiomech.2007.03.015.